Version of Record: https://www.sciencedirect.com/science/article/pii/S1293255822000851
Manuscript_f3fb7960c781fa8c831b5e9069296933

Mesoporous MoO_2 Thin Films for High Rate Li^+ Storage: Effect of Crystallinity and Porous Structure

Yan Yan[a], Hyung-Seok Kim[b,#], John B. Cook[a], Shauna Robbennolt,[a] Bruce Dunn,[b,c] Sarah H. Tolbert[a,b,c,*]

[a] Department of Chemistry and Biochemistry, UCLA, Los Angeles, California 90095-1569, United States

[b] Department of Materials Science and Engineering, UCLA, Los Angeles, California 90095-1595, United States

[c] The California NanoSystems Institute, UCLA, Los Angeles, California 90095

[#] Current address: Center for Energy Storage Research, Korea Institute of Science and Technology, Hwarang-ro 14-gil 5, Seongbuk-gu, Seoul 136-791, Republic of Korea

Abstract:

MoO_2 has attracted much recent attention as a high capacity energy storage material. While much of the current work on MoO_2 has been focused on the high capacity four-electron reduction, this reaction is limited to slow charging process due to the large volume change and phase transitions involved. In this study we focus on one-electron insertion reactions and demonstrate that ordered mesoporous thin films of MoO_2 can show signatures of pseudocapacitive charge storage. Mesoporous MoO_2 (mp-MoO_2) thin films were treated at different temperatures between 350 and 700 °C to explore the role of crystallinity and nanoscale structure on charging dynamics. The porosity and pore size decreased while the crystallinity and grain size increased as the calcination temperature increased. Materials processed at 600 °C showed the best electrochemical performance due to an optimized combination of high crystallinity and small grain size. These materials could be charged and discharged in 24 seconds while still achieving a Li^+ storage capacity of 158 mAh/g. While such thin film systems do not constitute a practical energy storage

device, the work provides structural design parameters for the production of future bulk nanoporous materials.

Graphic Abstracts

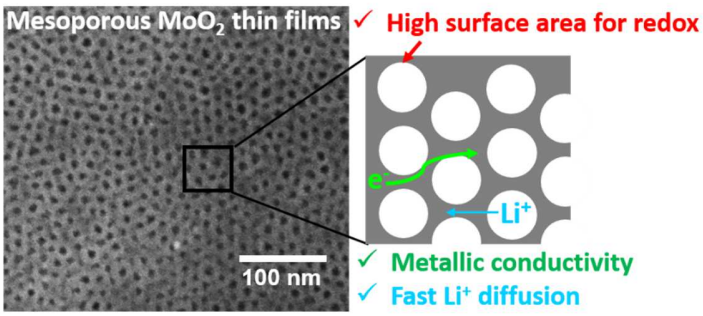

Research Highlights:

We successfully synthesized mesoporous MoO_2 thin films with controlled porosity, pore size and crystallinity.

Mesoporous MoO_2 thin films demonstrate excellent rate capability. More than 158 mAh/g charge storage achieved within 24 seconds in optimized electrode.

Kinetic analysis based on cyclic voltammograms show signatures of pseudocapacitive behavior

Keywords: *MoO_2, pseudocapacitor, electrochemical-energy storage, mesoporous, Li-ion battery.*

1. Introduction

Pseudocapacitive charge storage is emerging as an exciting alternative technology to traditional Li-ion batteries due to the potential to retain reasonably high energy density at high power density. Many applications can be envisioned, ranging from portable electronics to hybrid vehicles. One fundamental difference between pseudocapacitive materials and Li-ion battery materials lies in the lengthscale for ionic diffusion process. Both systems generally involve faradaic (i.e. charge transfer or redox) reactions, but Li-ion battery electrodes combine these reactions with solid-state ionic diffusion (10^{-10} - 10^{-15} cm^2/s) through the bulk material, which intrinsically leads to slow charging and discharging times [1,2]. In contrast, pseudocapacitive materials utilize those same faradaic reactions at or near the surface of a material, where the fundamental kinetic barriers associated with solid-state diffusion processes are avoided [3–6]. The charge storage arising from redox reactions in battery and pseudocapacitive materials is entirely different from that which occurs in carbon-based supercapacitor materials which store charge in the electric double layer through a non-faradic process and are termed electrical double layer capacitors (EDLCs). EDLCs store energy by physically adsorbing ions at the interface between the electrode and electrolyte. They are intrinsically fast as no charge transfer or solid-state ion diffusion is involved, but the amount of energy stored is limited and highly dependent on surface area [6,7]. Overall, pseudocapacitive materials can potentially combine the energy density of batteries with the power density of EDLCs, and it is for this reason, they have been widely researched for use in next generation energy storage devices.

Molybdenum dioxide (MoO_2) has been studied as a promising negative electrode material for lithium ion batteries because of its low metallic resistivity (8.8×10^{-5} Ω cm at 300 K), high capacity (840 mAh/g when discharged to 0 V *vs*. Li/Li^+), and high density (6.5 g/cm^3) [8,9]. Li^+

ion-based charge storage in MoO_2 occurs via two different mechanisms: (1) Li^+ ion insertion/deinsertion between 1.0 to 3.0 V (*vs*. Li/Li^+), and (2) a conversion reaction below 1 V(vs. Li/Li^+)[10].

$$xLi + MoO_2 = Li_xMoO_2,\ 0 < x < 0.98,\ \text{Capacity} = 210\ \text{mAh/g} \quad (1)$$

$$Li_{0.98}MoO_2 + 3.02Li = 2Li_2O + Mo,\ \text{Capacity} = 630\ \text{mAh/g} \quad (2)$$

Although the conversion reaction in MoO_2 leads to a much higher theoretical capacity compared to the 1-electron insertion/deinsertion process, the conversion process is generally slow due to the large volume expansion that occurs during conversion [11,12]. Furthermore, the transition from MoO_2 to Mo is kinetically hindered and destroys the parent structure in an irreversible manner [13,14].

On the other hand, the one-electron insertion process shown in equation 1 is much more facile. Monoclinic MoO_2 (space group of P21/c(14)) has a rutile-type tunnel structure framework which consists of MoO_6 octahedra, linked to form one dimensional channels along the a-axis where Li-ions can be inserted and extracted reversibly [15]. The insertion process is thus a more promising mechanism for pseudocapacitive energy storage.

Various structures and morphologies of MoO_2, such as nanorods [8], nanobelts [16], nanosheets [17], nanowires [18], nanotubes [19,20], nanoparticles [12,21], porous structure [22–24] and hierarchical architectures [25] have been reported using high temperature vapor deposition, thermal reduction, electrochemical deposition and hydrothermal synthesis. However, most of these materials have been studied as conversion-type electrodes and have limited application as fast charging electrodes. MoO_2 nanoparticles used as insertion hosts with diameters of 15-20 nm diameters were reported to a show high capacity for lithium (120 mAh/g) at 10C [12].

However, large amount of MoO_3 on the nanoparticle surface resulted in poor electrical connection between individual nanoparticles, which hindered charge storage at faster rates. Growing MoO_2 directly onto a conductive scaffold such as graphene [12,26] was found to limit these resistive effects, but it involves extra reagents and is less scalable.

In this work, instead of using a graphene scaffold, we use polymer templating methods to build our nanoscale MoO_2 into a mesoporous network that can alleviate the impact of surface oxide by creating an electrically interconnected conductive backbone. Related templated mesoporous structures have already been widely used as energy storage materials, such as TiO_2 [27], $LiCoO_2$ [28], $LiMn_2O_4$ [29], Nb_2O_5 [30], MoS_2 [31]. They offer several advantages, including: (1) high capacity from the large number of surface redox sites that arise due to the high surface area that results from small nanoscale domains; (2) short solid-state diffusion lengths for ions due to the nanosized walls; and (3) efficient electrolyte access through the mesoporous channels. These qualities are beneficial for achieving high capacity for lithium ions at high charge/discharge rates. The templating method allows for precise control of porosity and pore size, which can affect the fraction of surface sites as well as the solid-state diffusion length, and thus further impacts the capacity and kinetics of a system [32–38]. Stucky *et al.* have previously synthesized mesoporous MoO_2 using SBA 15 as a hard template [9,22]. Ordered porous nanostructures and very high capacities were obtained when discharged to 0.1 V *vs*. Li/Li^+. Up to 1800 mAh/g capacity was achieved by utilizing Li^+ storage sites at the interface of Li_xMoO_2 nano-domains and forming Li-rich domains [22]. The very promising kinetics of 1-electron insertion into mesoporous MoO_2 has not, however, been discussed.

Crystallinity can also have a significant impact on charge storage. Previous research [39,40] has shown that crystalline materials outperformed amorphous ones due to the extra

capacity arising from intercalation pseudocapacitance in crystalline materials, whereas the capacity in amorphous samples was limited to surface redox pseudocapacitance. Different crystalline phases also provide different Li^+ transport pathways, which can further influence the capacity and rate capabilities [40]. High temperature calcination is a typical route to enhancing crystallinity [41–43] and thus improving the electrochemical performance, but it can also cause coarsening of the nanoscale architecture [44].

In this work we fabricate ordered mesoporous MoO_2 (mp-MoO_2) thin film electrodes to study the correlation between their charge storage behavior and their crystallinity and porous structure. The thin film format was chosen to eliminate the need for carbon additives or binders in order to isolate the role of atomic and nanoscale structure in controlling the charge storage properties of nanostructured MoO_2. Evaporation induced self-assembly (EISA) of block copolymer templated sol-gel type precursors is a well-established method to synthesize a variety of ordered mesoporous materials with uniform, well-defined pore sizes [39,45–49]. This synthesis method leads to nanocrystalline domains which are directly connected to each other, allowing for charge storage with reduced limits from electrical resistance. The ability to control the pore size and pore-size distribution further enables optimized electrolyte diffusion [50]. In this report, several mesoporous architectures were prepared using different heating conditions to vary the crystallinity and porous structure. The nanostructures were correlated with pseudocapacitive signatures using a detailed cyclic voltammetric analysis that quantitatively decouples capacitive-driven and diffusion-controlled contributions to the overall charge storage. This analysis allows us to directly explore the role of nanoscale architecture in controlling electrochemical kinetics.

2. Material and Methods

2.1 Materials

The following materials were obtained from commercial suppliers and used without further purification: molybdenum (V) chloride (99.6% metal basis, Alfa Aesar), poly(butylene oxide)-block-poly(ethylene oxide) (PBO(5000)-b-PEO(6500), Mn = 11500, PDI=1.06-1.15, Advanced Polymer Materials Inc).

2.2 Synthesis of MoO_2

In a typical synthesis, 0.015 g of PEO-b-PBO was first dissolved in 2 mL ethanol. Then, 0.2 g $MoCl_5$ was added. The resulting sol was stirred for 2 h prior to film deposition. Thin films were deposited via dip-coating on polar substrates such as silicon and platinum coated Si (3 nm Ti-150 nm Pt- 360 nm SiO_2- Si). Optimal conditions included 4% relative humidity and a constant withdrawal rate of 3 mm/s. The films were aged at 180 °C for 12 h prior to template removal to prevent loss of mesoscale order during the course of template removal and crystallization. Films were calcined using a 5 °C/min ramp to selected temperatures (350 °C, 500 °C, 600 °C and 700 °C) in 5%/95% H_2/N_2 reducing atmosphere to yield the crystalline, porous MoO_2.

2.3 Characterization

Scanning Electron Microscopy (SEM) images were obtained using a model JEOL JSM-6700F field emission electron microscope with a 5 kV accelerating voltage and secondary electron detector configuration. Transmission Electron Microscopy (TEM) images were obtained using a Tecnai T12 Quick Cryo-electron microscope at an accelerating voltage 120 kV and a Gatan 2k×2k CCD detector. Ellipsometric porosimetry was performed on a PS-1100 instrument from Semilab using toluene as the adsorbate. The instrument used a UV-visible CCD detector adapted to a

grating spectrograph to analyze the signal reflected by the sample. The light source was a 75 W Hamamatsu Xenon lamp and the measurements were performed in the spectral range from 1.25–4.5 eV. Data analysis was performed using the associated Spectroscopic Ellipsometry Analyzer software with the assumption of cylindrical pores. Two-dimensional small-angle and wide angle X-ray scattering data were collected at the Stanford Synchrotron Lightsource (SSRL) using beamlines 1-5 and 11-3, respectively. Beamline 1-5 was operated at 10.000 KeV using the Rayonix-165 CCD detector. Beamline 11-3 was operated at 12.735 KeV using a MAR345 imaging plate (345 mm diameter). XPS analysis was performed using a Kratos Axis Ultra DLD with a monochromatic Al (Kα) radiation source. The charge neutralizer filament was used to control charging of the sample, a 20 eV pass energy was used with a 0.05 eV step size, and scans were calibrated using the C 1s peak shifted to 284.8 eV. The integrated area of the peaks was found using the CasaXPS software, and atomic ratios were also found using this software. The atomic sensitivity factors used were from the Kratos library within the Casa software.

2.4 Electrochemistry measurements

The as prepared mp-MoO_2 thin films on Pt-coated silicon substrates were used as working electrodes. Electrochemical measurements of these thin film electrodes were carried out in a three-electrode cell with 1M $LiClO_4$ in propylene carbonate as electrolyte; lithium foils were used as the counter and reference electrodes. The mp-MoO_2 thin films were cycled between 1.1 to 3.0 V *vs.* Li/Li^+ to investigate the capacity and kinetics of mp-MoO_2 using an Arbin BT-2000. All tests were performed in an argon or nitrogen filled glovebox. Inductively coupled plasma optical emission Spectrometry (ICP-OES) was used to determine thin film masses. The mp-MoO_2 thin films were dissolved in 2.9 M NH_4OH (28~30 wt%, Sigma-Aldrich) aqueous solution overnight at room temperature followed by HotBlock (SC100, Environmental Express) heating at 95 °C to nearly

dryness. After adding 2% (v/v) HNO_3 aqueous solution and extracting the analytes at 95 °C for 3 h, the samples were cooled down and analyzed with Inductively Coupled Plasma Optical Emission Spectrometry (ICPE-9000, Shimadzu, Japan). The calculated areal loading from several films is 43 $\mu g/cm^2 \pm 2\ \mu g/cm^2$, which is used for the determination of the mass normalized capacities in this report.

3. Results and Discussion

3.1. Materials characterization

Ordered mesoporous MoO_2 thin films (mp-MoO_2) with thickness around 250 nm were synthesized through evaporation induced self-assembly (EISA) of molybdenum precursors and an amphiphilic block copolymer (poly(ethylene oxide-block-butylene oxide), PEO-b-PBO), followed by a heat treatment in N_2/H_2 (95 vol%/5 vol%) to remove the template and crystalize the structure. PEO-b-PEO was used because its high oxygen content allows for removal of template in a reducing atmosphere, which is needed to directly crystalize MoO_2 without forming MoO_3. Back conversion of MoO_3 to MoO_2 tends to degrade the pore structure due to the large volume change and structural evolution (orthorhombic to monoclinic), and so a direct heat treatment method to remove template and crystalize the mp-MoO_2 structure at one time is desirable.

To examine the porous structure, we have utilized scanning electron microscopy (SEM), transmission electron microscopy (TEM), small angle X-ray diffraction, and porosimetry methods. Films synthesized at 350 °C, 500/600 °C and 700 °C showed clear differences in behavior, but films synthesized at 500 °C and 600 °C showed almost identical structural and electrochemical performance. Because of this, only one of these samples was chosen for further characterization. For the remained of the manuscript, 350 °C, 600 °C and 700 °C treated samples were used for comparison, but structural and electrochemical data for the 500 °C treated sample can be found in

SI figures S1 and S3 and in Table 1. Figures 1a – 1c display SEMs image of calcined mp-MoO_2 films that shows the surface of an ordered porous structure with ~10 nm pores and ~10 nm walls. As the calcination temperature increases, the wall thickness slightly increases due to grain growth.

Figures 1d – 2f show toluene adsorption/desorption isotherms and the derived pore size distribution. The isotherms show a large hysteresis between adsorption and desorption of toluene, which is indicative of a mesoporous structure with a cage and neck type structure. The porosity calculated from the total absorption volume is 31%, 26% and 18%, respectively, for mp- MoO_2 calcined at 350 °C, 600 °C and 700 °C. Using the adsorption isotherm, the average pore size of the mp-MoO_2 thin film is calculated to be 8.5 nm, 7.8 nm and 6.5 nm, respectively, values that gradually decrease as the calcination temperature increases. This indicates that the porous structure shrinks at higher temperature. These values are in excellent agreement with the SEM data in Fig. 1a–1c. We note that only pore size, and not surface area, is reported because this data was collected using toluene porosimetry at room temperature. Toluene is not at its liquid-vapor equilibrium point at room temperature, and so the BET region, which is normally used to calculate surface area is compressed and thus surface area cannot be extracted from data.

A TEM image (Fig. 1g) also corroborates the porous structure in MoO_2 mesoporous thin film calcined at 600 °C. Additional high and medium resolution TEM images can be found in the SI in figure S2. The low resolution data provides an addition view of the mesoscale structure, while the medium resolution image allows for direct visualization of the size of the crystalline grains within the framework. Finally, synchrotron-based grazing incidence small angle scattering (GISAXS) (Fig. 1h and 1j) was used to further characterize both the size and periodicity of the porous architecture. The data show diffraction arcs along the q_{xy} direction for both mp-MoO_2-600 and mp-MoO_2-700, demonstrating that these thin films have ordered porosity in the plane of the

substrate. The in-plane repeating distances calculated from q_{xy} (as $q_z \rightarrow 0$) in Fig. 1h and 1j are 22 nm and 18 nm, which matches observations from SEM. These ordered porous structure thus provides enhanced surface area and good electrolyte accessibility for high rate charge storage, combined with nanoscale pore walls to ensure short solid-state diffusion length.

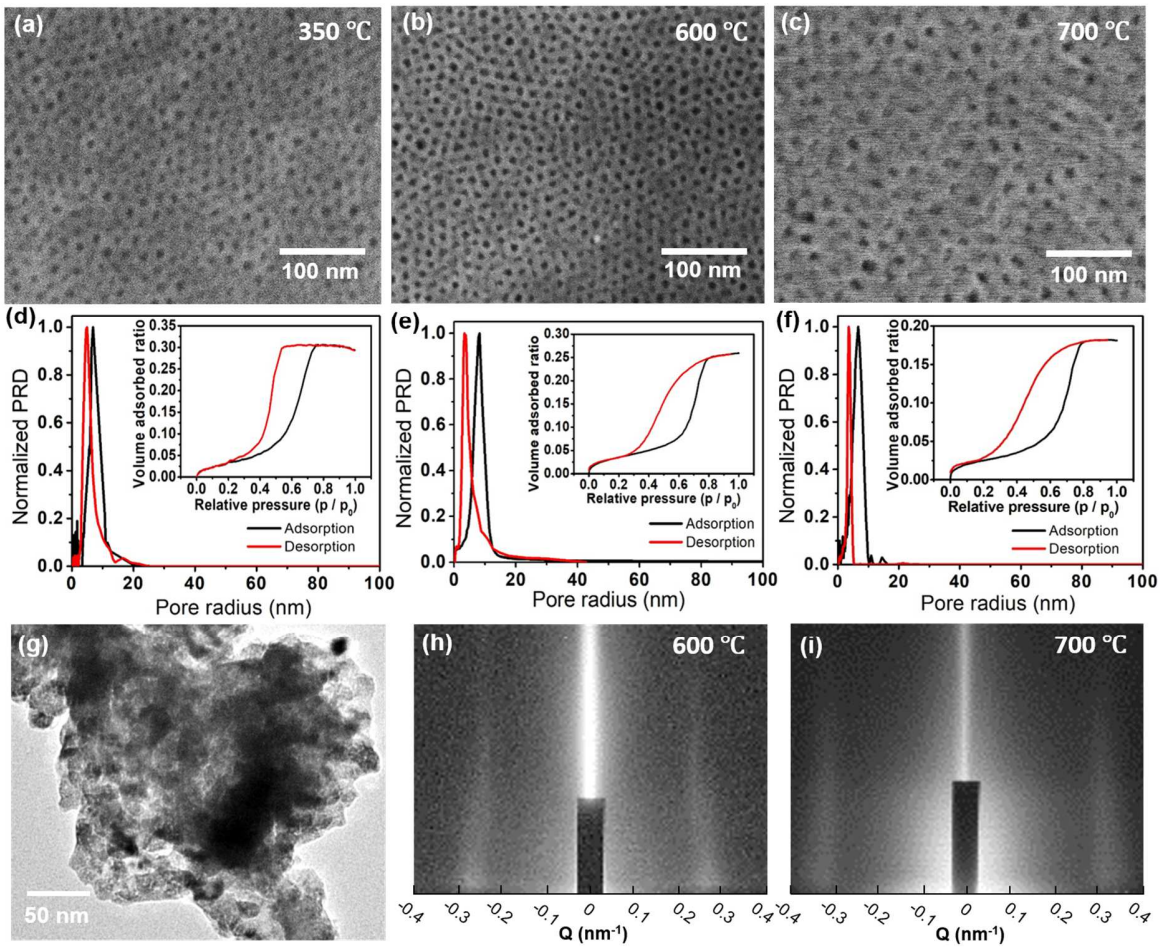

Fig. 1. Structural characterization of mesoporous MoO_2 thin films. (a-c) SEM images of the surface of a MoO_2 mesoporous thin films calcined at (a) 350 ℃, (b) 600 ℃ and (c) 700 ℃. All structures show open porosity. (d-f) Toluene adsorption-desorption isotherms and corresponding pore size distribution data obtained from the isotherms for MoO_2 mesoporous thin films calcined at (d) 350 ℃, (e) 600 ℃ and (f) 700 ℃. As the calcination temperature increases, grain growth in the structure leads to lower porosity and smaller pore size. (g) TEM image of mp-MoO_2-600. (h) and (i) Synchrotron grazing incidence small angle x-ray scattering patterns for MoO_2 calcined at (h) 600 ℃ and (i) 700 ℃. The in-plane repeat distance is 22 nm and 18nm, respectively, for the two samples.

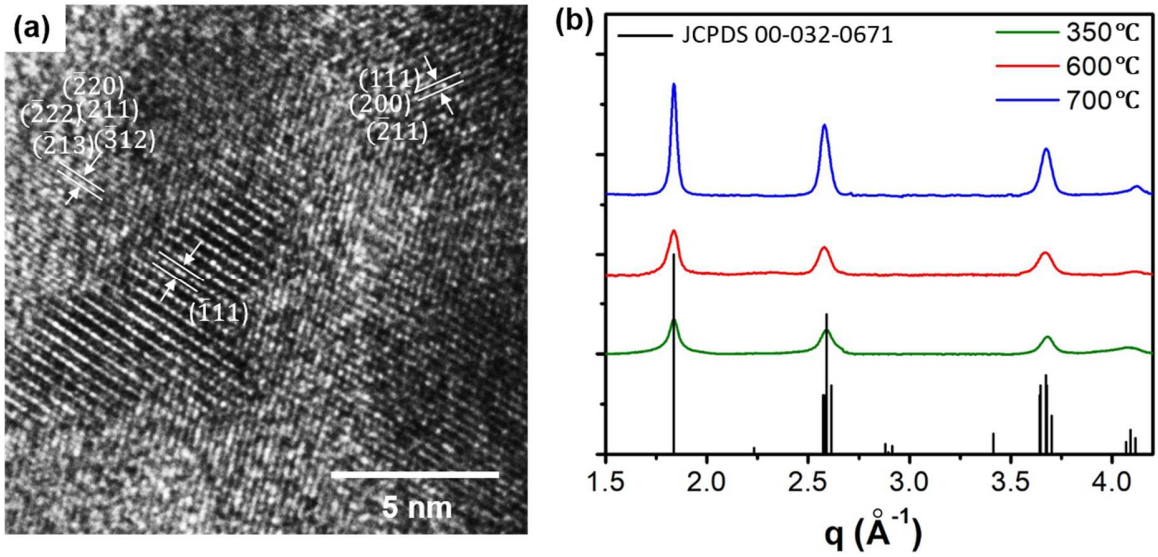

Fig. 2. Crystal structure of mesoporous MoO_2 thin films. (a) HRTEM image of a 600 ℃ calcined MoO_2 mesoporous thin film. The lattice spacing of monoclinic MoO_2 can be observed. (b) Synchrotron grazing incidence wide angle x-ray scattering pattern of MoO_2 calcined at different temperatures. All materials show phase pure material with peaks indexed to monoclinic MoO_2 (JCPDS No. 032-0671).

The crystal structure of mp-MoO_2 was analyzed using high-resolution TEM (HRTEM) and synchrotron-based grazing incidence wide angle X-ray scattering (GIWAX). In the HRTEM image (Fig. 2a), the lattice spacing of monoclinic MoO_2 can be observed. Fig. 2b shows the 1-D GIWAX patterns integrated from the 2-D images of mp-MoO_2-350, mp-MoO_2-600 and mp-MoO_2-700. All patterns match JCPDS card No. 32-0671 for monoclinic MoO_2. The monoclinic phase is known to be a metallic conductor [15,23] due to the Mo-Mo pairing along the Mo atom chains. The unique structure also has potential for fast Li^+ conduction through octahedral interstitial sites in the "tunnels" between the Mo chains [51]. Although the three samples all display diffraction peaks for the monoclinic phase, the samples prepared at higher temperature were more crystalline, based on the diffraction intensities. Based on peak width, we can calculate the crystallite sizes to be 11 nm, 13 nm and 18 nm, respectively, for samples heated between 350 and 700 °C. The details of peak

widths and calculated domain sizes can be found in Table 1. We believe the grain size plays an important role in determining charge storage behavior, as discussed later.

Table 1: Diffraction peak widths and crystalline domain sizes for all samples examined in this work.

Calcination Temperature (°C)	FWHM ($Å^{-1}$)	Crystallite Size (nm)
350	0.77	11
500	0.67	13
600	0.64	13
700	0.48	18

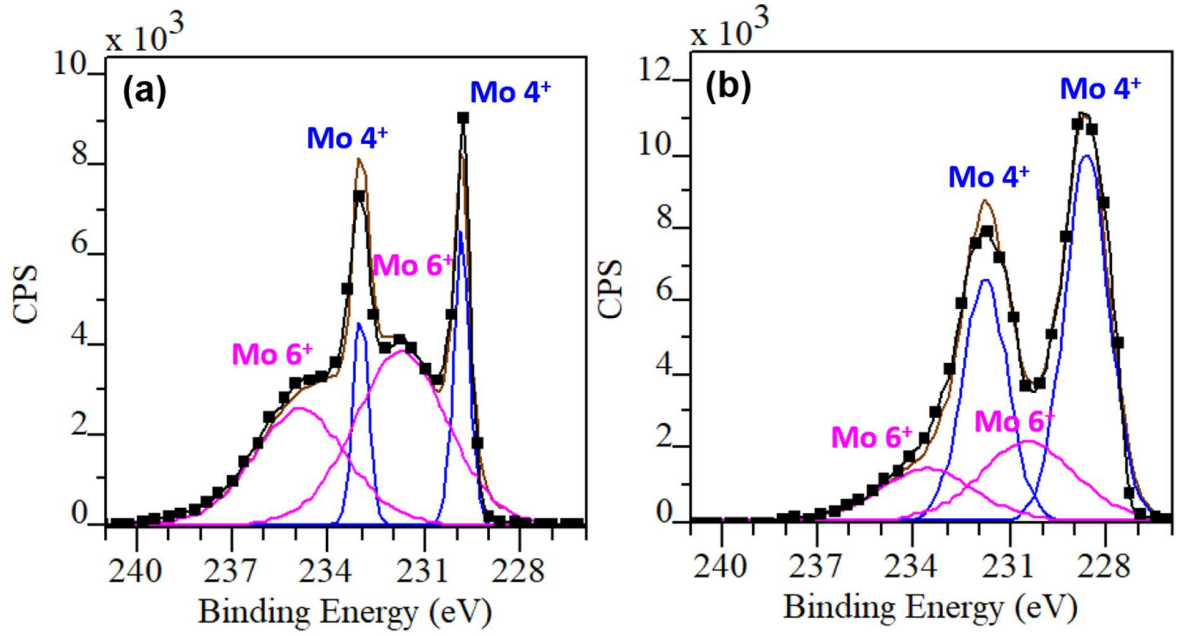

Fig. 3. X-ray photoelectron spectra obtained to analyze the surface oxidation state of mesoporous MoO_2 (a) pristine and (b) after Ar ion etching. Mo^{6+} peaks correspond to a surface oxide, which is removed by etching.

X-ray photoelectron spectroscopy (XPS) measurements were performed to study the chemical composition and oxidation state of the material. Fig. 3a shows high resolution XPS traces

for the Mo 3d core level. The Mo 3d peak is composed of 2 sets of the spin-orbit doublets corresponding to Mo $3d_{3/2}$ and Mo $3d_{5/2}$. The peaks at 229.8 eV and 233.0 eV are attributed to Mo^{4+} and those at 231.7 eV and 234.9 eV are attributed to Mo^{6+}. Since the probing depth of XPS is only a few nanometers, this indicates the surface of MoO_2 is mostly MoO_3. Fig. 3b shows XPS traces for Mo 3d after Ar etching, which was used to remove the surface layer. The Mo^{4+}/Mo^{6+} ratio calculated from the peak area changed from 0.29 to 2.2 after etching, revealing that the majority of the nanostructure backbone is composed of MoO_2. Despite the surface oxidation, the mesoporous framework consists of interconnected conductive MoO_2 grains and so the overall resistance through the network should be low. This is a key advantage of using a mesoporous network, rather isolated MoO_2 nanocrystals.

3.2. Electrochemistry

Mp-MoO_2 films were cycled in a 3-neck flooded cell between 1.1 and 3 V *vs*. Li/Li^+ to examine the one-electron insertion process. As the electrochemical activity highly depends on the crystallinity of the structure, the three samples made at different temperatures and characterized above were compared. Fig. 4 shows the cyclic voltammograms (CV) of these electrodes under different scan rates varying from 1 mV/s to 100 mV/s. All three samples display the signature redox peaks at 1.27 V and 1.55 V (Li insertion) and 1.34 V and 1.66 V *vs*. Li/Li^+ (Li extraction) for monoclinic MoO_2. In the bulk, these peaks have been associated with a phase transitions from the monoclinic MoO_2 (at low Li content) to orthorhombic MoO_2 and back to monoclinic (at high Li content), [15] but they still occur in nanoscale materials that show full supression of these phase transitions [12]. The peaks are sharper in the samples prepared at the higher temperature, indicating a more crystalline structure. In general, as the scan rate increases, the shift between the anodic and cathodic pair of peaks increase as it gets more difficult to efficiently access the active sites during

the shorter time frame. Nevertheless, the higher temperature crystalized structure displays smaller peak shifts and polarization effect. This suggests that the sample prepared at higher temperature has less lattice defects, which could allow for faster lithium insertion through the tunnel sites.

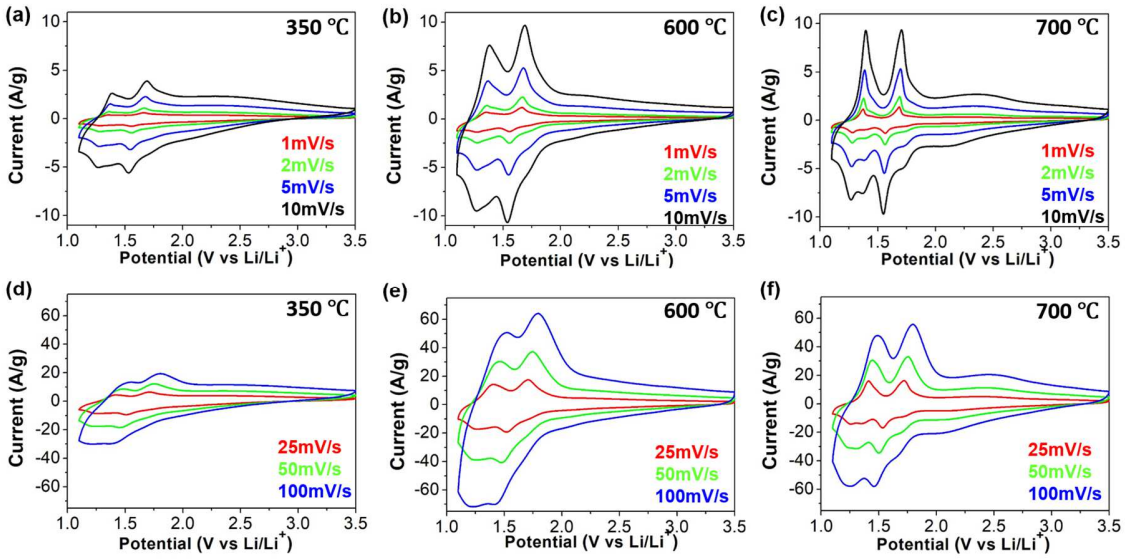

Fig. 4. Cyclic voltammograms of mesoporous MoO_2 thin films calcined at different temperatures. (a) (d) mp-MoO_2-350, (b) (e) mp-MoO_2-600, and (c) (f) mp-MoO_2-700. CVs were taken at different scan rate. (a)-(c) 1 mV/s to 10 mV/s and (d)-(f) 25 mV/s to 100 mV/s. As the calcination temperature increases, the characteristic redox peaks become more defined, and the voltage separation between anodic and cathodic peaks decreases.

The rate capabilities of mp-MoO_2-350, mp-MoO_2-600 and mp-MoO_2-700 were analyzed with cyclic voltammograms at different scan rates. Fig. 5a and 5b plot the specific capacity in the three samples as a function of scan rate and charge time, respectively. Data similar to Figure 5a, but including the sample calcined at 500 °C is shown in SI figure S3. In agreement with the structural data, the samples calcined at 500 and 600 °C show nearly identical behavior. The data in Figure 5 indicate that mp-MoO_2-600 has the highest initial capacity, 253 mAh/g at 1 mV/s. Mp-MoO_2-700 has a similar initial capacity of 239 mAh/g. The capacities are higher than the theoretical one-electron insertion capacity of 209 mAh/g, which is likely due to a combination of

some double layer capacitance from the high surface area mesoporous structure and some additional redox sites at the surface of the porous material. Mp-MoO_2-350 has only 200 mAh/g capacity at 1 mV/s, most likely because not all the redox sites are accessible due to the low crystallinity. Mp-MoO_2-350 also has the worst rate capability, likely for the same reason. The defects or amorphous regions in the structure may prevent full utilization of the 1-D tunnel sites for insertion. Mp-MoO_2-600 has the highest capacity retention at fast scan rates, with over 60% (158 mAh/g) of the initial capacity accessed within 24 seconds. This could be the result of an ideal nanostructure consisting of interconnected nanocrystals with short ion diffusion lengths and good electrolyte accessibility combined with high electrical conductivity in the connected backbone. Mp-MoO_2-700 has slightly worse kinetics and capacity. This is probably due to the larger crystallite size in Mp-MoO_2-700 which leads to slightly thicker wall and longer solid-state diffusion.

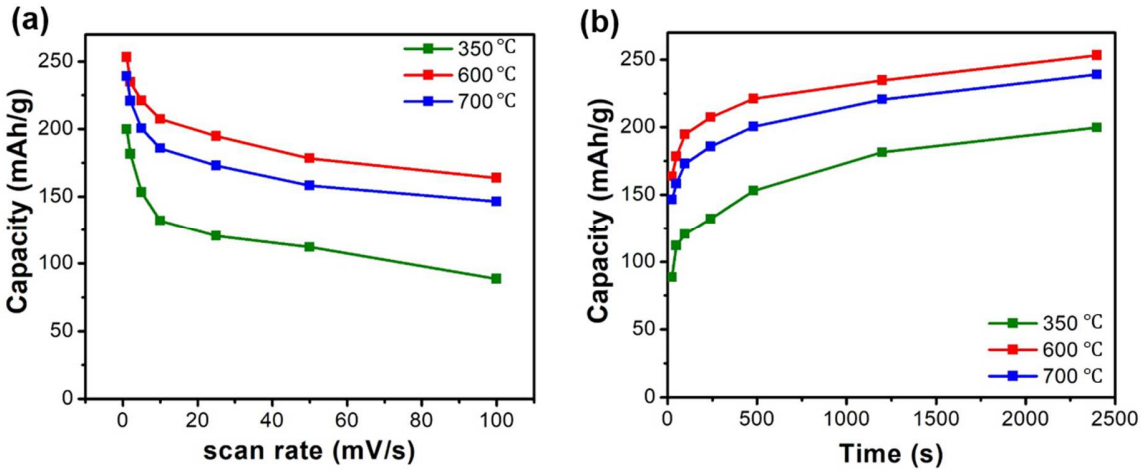

Fig. 5. Rate capabilities of mesoporous MoO_2 thin films calcined at different temperatures. (a) Specific capacity as a function of scan rate and (b) specific capacity as a function of scan time obtained from CV. Mp-MoO_2-600 displays the best kinetic behavior with more than 60% capacity retention at 100 mV/s or within 24 seconds.

To better understand the effect of crystallinity on electrochemical performance in MoO_2, we analyzed the dependence of peak currents on scan rates. Generally, the current (i) varies with the scan rate (v) according to the following equation:

$$i = av^b \quad (3)$$

where a and b are constants. The value of b can vary between 0.5 and 1, with a b-value of 0.5 indicating a diffusion-controlled process and a b-value of 1 representing capacitive behavior [30,52]. Fig. 6a – 6c shows plots of log(i) versus log(v) from 1 to 20 mV/s for the four redox peaks in each sample. Overall, mp-MoO_2-600 sample has the highest b value while mp-MoO_2-350 has the lowest. The low b values in mp-MoO_2-350 can be attributed to the low crystallinity of the structure. The existence of defects or amorphous areas can block efficient Li^+ insertion through the 1D tunnel, and this type of reduction in Li^+ diffusion has been observed previously in nanostructured electrode materials with secondary phase inclusions [53]. Interestingly, mp-MoO_2-700 also has lower b values than mp-MoO_2-600, despite the higher crystallinity. This is most likely due to the larger crystallite size in mp-MoO_2-700, which increases the solid-state diffusion length and therefore results in more diffusion-controlled contributions to the total capacity. The mp-MoO_2-600 sample appears to be the best compromise, having better crystallinity than mp-MoO_2-350 materials and thinner walls than mp-MoO_2-700 samples. It thus showed the best electrochemical performances among the three samples.

The different kinetic behaviors in the three samples can also be analyzed with a related method, in which the total current measured in a CV experiment is decomposed into a purely capacitive and pure diffusion-controlled contribution to provide an approximation of the capacitive charge storage fraction. Here the current response is considered to be comprised of a capacitive

current (which vary as $k_1 v$) and diffusion-controlled current (which vary as $k_2 v^{0.5}$), as shown in equation (4).

$$i(V) = k_1 v + k_2 v^{0.5} \quad (4)$$

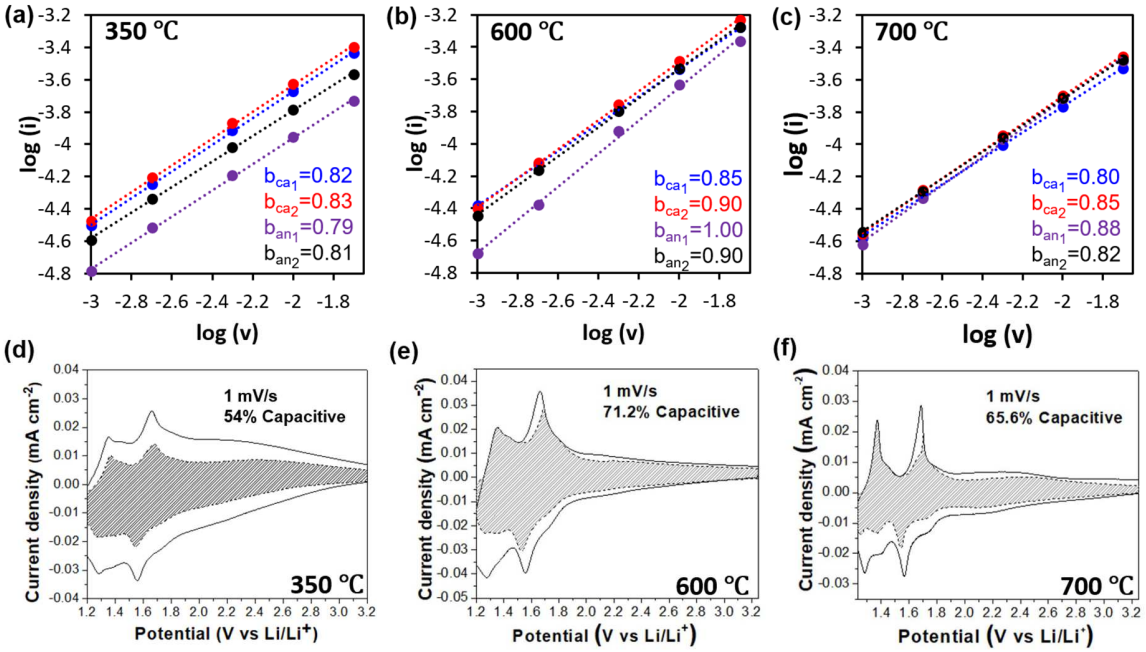

Fig. 6. Analysis of pseudocapactive behaviors in mesoporous MoO_2 thin films calcined at different temperatures. (a)-(c) Plots of log(peak current) vs log(sweep rate) used to obtain b-values for MoO_2 redox peaks using CV curves obtained by scanning between 1.1 – 3.5 V vs Li/Li+ at scan rates of 1-20 mV/s. (a) mp-MoO_2-350, (b) mp-MoO_2-600 and (c) mp-MoO_2-700. (d)-(f) Capacitive charge storage contributions for mp-MoO_2 cycled at 1 mV/s calculated using the method described in Equation (4) for (d) mp-MoO_2-350, (e) mp-MoO_2-600 and (f) mp-MoO_2-700. The film calcined at 600 °C has both the highest b value and the largest capacitive contribution, suggesting dominantly pseudocapacitive behavior.

Here *i(V)* is the current at any given voltage *V*, and *v* is the scan rate. Fig. 6d – 6f show plots of the capacitive and diffusion-controlled fraction for each sample at a slow sweep rate of 1 mV/s where both capacitive and diffusion-controlled reactions should be fully accessible. Analysis using equation (4) indicates that 71% of the current in mp-MoO_2-600 is capacitive, in contrast to 65% for mp-MoO_2-700 and 54% for mp-MoO_2-350. Interestingly, we find that the voltage regions near the cathodic peaks in the insertion process are more diffusion controlled than the extraction process.

Overall, both kinetic analyses indicate that the mp-MoO_2-600 sample displays the most capacitive behavior, likely due to a combination of high crystallinity and small grain size. This capacitive behavior allows mp-MoO_2-600 to show the best overall charge storage kinetics at fast rates. While we fully acknowledge that these thin film systems are not practical electrodes due to their very low mass loading, it is hoped that the architectural design parameters established in this work will be helpful for the future design of mesoporous MoO_2 powders that can be fabricated into traditional thick film electrodes.

4. Conclusions

We have demonstrated that ordered porous MoO_2 can be synthesized via a block copolymer template method. The porosity, pore size and crystallinity can be controlled using different heating conditions. GISAXS, SEM, TEM and porosimetry confirm the ordered porous structure with ~30% porosity and 15-20 nm pore size. GIWAXS indicates that all three samples have the monoclinic MoO_2 crystalline phase, which is known to be electrically conductive, with 10-20 nm average grain sizes, depending on the calcination temperature. The combination of these structural factors leads to fast kinetics for Li^+ charge storage. The three samples prepared at different temperature were then compared for their electochemical performance. Mp-MoO_2-600 appears to have the optimal combination of high crystallinity and thin walls that provide short Li-ion diffusion lengths. Over 60% (158 mAh/g) of the capacity can be accessed in only 24 seconds in mp-MoO_2-600. Kinetic analysis using cyclic voltammogram further confirms that the mp-MoO_2-600 shows the most pseudocapacitive behavior with b values ranging from 0.9-1 for the various redox peaks and >70% capacitive current contribution at 1 mV/s.

Overall, we have demonstrated that mp-MoO_2 is a redox-based charge storage material with fast kinetics. While we reiterate that we do not consider these thin films to have potential as

practical energy storage systems, it should be possible to create nanoporous powders with similar pore sizes, wall thicknesses, and crystallinity that could be built into typical slurry electrodes with much higher mass loadings. Based on the work presented here, such systems should also achieve good kinetics based on their electrically interconnected conductive network, their ideal nano architecture for electrolyte accessibility, and their short solid-state ion diffusion length.

Acknowledgements

Authors Y.Y. and S.H.T acknowledge support from U.S. Department of Energy (DOE), Office of Science, Basic Energy Sciences under Award Number DE-SC0014213 (materials synthesis, characterization, electrochemical characterization, data analysis, and manuscript preparation). H-S.K. and B.D. acknowledge support from the Office of Naval Research under Award N00014-16-1-2164 (electrochemical kinetics studies). Y.Y. acknowledges support from Chinese Scholar Council (initial synthetic work). This work made use of instruments TEM facilities at the Electron Imaging Center for NanoMachines supported by NIH (1S10RR23057) and the ICP-MS facility within the UC Center for Environmental Implications of Nanotechnology, both located in the CNSI at UCLA. This manuscript contains X-ray diffraction data collected at the Stanford Synchrotron Radiation Lightsource. Use of the Stanford Synchrotron Radiation Lightsource, SLAC National Accelerator Laboratory, is supported by the U.S. Department of Energy, Office of Science, Office of Basic Energy Sciences, under Contract DE-AC02-76SF00515.

Author information

Corresponding Author
E-mail: tolbert@chem.ucla.edu

Declaration of Competing Interest:

The authors declare no competing interests.

References

[1] M. Park, X. Zhang, M. Chung, G.B. Less, A.M. Sastry, A review of conduction phenomena in Li-ion batteries, J. Power Sources. 195 (2010) 7904–7929.

https://doi.org/10.1016/j.jpowsour.2010.06.060.

[2] N. Balke, S. Jesse, a N. Morozovska, E. Eliseev, D.W. Chung, Y. Kim, L. Adamczyk, R.E. García, N. Dudney, S. V Kalinin, Nanoscale mapping of ion diffusion in a lithium-ion battery cathode., Nat. Nanotechnol. 5 (2010) 749–54. https://doi.org/10.1038/nnano.2010.174.

[3] P. Simon, Y. Gogotsi, B. Dunn, Materials science. Where do batteries end and supercapacitors begin?, Science. 343 (2014) 1210–1. https://doi.org/10.1126/science.1249625.

[4] B.E. Conway, TECHNICAL PAPERS' ELECTROCHEMICAL SCIENCE AND TECHNOLOGY Transition from "Supercapacitor" to "Battery" Behavior in Electrochemical Energy Storage, Electrochem. Sci. Technol. 138 (1991) 1539–1549.

[5] B.E.E. Conway, V. Birss, J. Wojtowicz, The role and utilization of pseudocapacitance for energy storage by supercapacitors, J. Power Sources. 66 (1997) 1–14. https://doi.org/10.1016/S0378-7753(96)02474-3.

[6] B.E. Conway, W.G. Pell, Double-layer and pseudocapacitance types of electrochemical capacitors and their applications to the development of hybrid devices, J. Solid State Electrochem. 7 (2003) 637–644. https://doi.org/10.1007/s10008-003-0395-7.

[7] Y. Zhu, S. Murali, M.D. Stoller, K.J. Ganesh, W. Cai, P.J. Ferreira, A. Pirkle, R.M. Wallace, K.A. Cychosz, M. Thommes, D. Su, E.A. Stach, R.S. Ruoff, Carbon-Based Supercapacitors, Science (80-.). 332 (2011) 1537–1541. https://doi.org/10.1126./science.1200770.

[8] B. Guo, X. Fang, B. Li, Y. Shi, C. Ouyang, Y.S. Hu, Z. Wang, G.D. Stucky, L. Chen, Synthesis and lithium storage mechanism of ultrafine MoO_2 nanorods, Chem. Mater. 24 (2012) 457–463. https://doi.org/10.1021/cm202459r.

[9] Y. Shi, B. Guo, S. a. Corr, Q. Shi, Y.-S. Hu, K.R. Heier, L. Chen, R. Seshadri, G.D. Stucky, Ordered Mesoporous Metallic MoO_2 Materials with Highly Reversible Lithium Storage Capacity, Nano Lett. 9 (2009) 4215–4220. https://doi.org/10.1021/nl902423a.

[10] J.H. Ku, Y.S. Jung, K.T. Lee, C.H. Kim, S.M. Oh, Thermoelectrochemically Activated MoO_2 Powder Electrode for Lithium Secondary Batteries, J. Electrochem. Soc. 156 (2009) A688. https://doi.org/10.1149/1.3141670.

[11] A. Chen, C. Li, R. Tang, L. Yin, Y. Qi, MoO_2-ordered mesoporous carbon hybrids as anode materials with highly improved rate capability and reversible capacity for lithium-ion battery., Phys. Chem. Chem. Phys. 15 (2013) 13601–10. https://doi.org/10.1039/c3cp51255j.

[12] H.-S. Kim, J.B. Cook, S.H. Tolbert, B. Dunn, The Development of Pseudocapacitive Properties in Nanosized-MoO_2, J. Electrochem. Soc. 162 (2015) A5083–A5090. https://doi.org/10.1149/2.0141505jes.

[13] H. Si, L. Sun, Y. Zhang, L. Wu, Y. Zhang, Y. Zhang, Enhanced pseudocapacitive energy storage properties of budding-branch like MoO_2@ C/CNT nanorods. Dalton Trans.49 (2020), 1637-1645. https://doi.org/10.1039/C9DT04391H.

[14] Y. Zhu, X. Ji, S. Cheng, Z. Y. Chern, J. Jia, L. Yang, H. Luo, J. Yu, X. Peng, J. Wang, W. Zhou, Fast energy storage in two-dimensional MoO_2 enabled by uniform oriented tunnels. ACS nano, 2019, 13(8), 9091-9099. https://doi.org/10.1021/acsnano.9b03324

[15] J.R. Dahn, W.R. McKinnon, Structure and electrochemistry of Li_xMoO_2, Solid State Ionics. 23 (1987) 1–7. https://doi.org/10.1016/0167-2738(87)90074-9.

[16] L. Yang, L. Liu, Y. Zhu, X. Wang, Y. Wu, Preparation of carbon coated MoO_2 nanobelts and their high performance as anode materials for lithium ion batteries, J. Mater. Chem. 22 (2012) 13148. https://doi.org/10.1039/c2jm31364b.

[17] J. Ni, Y. Zhao, L. Li, L. Mai, Ultrathin MoO_2 nanosheets for superior lithium storage, Nano Energy. 11 (2015) 129–135. https://doi.org/10.1016/j.nanoen.2014.10.027.

[18] L. Mai, F. Yang, Y. Zhao, X. Xu, L. Xu, B. Hu, Y. Luo, H. Liu, Molybdenum oxide nanowires: Synthesis & properties, Mater. Today. 14 (2011) 346–353. https://doi.org/10.1016/S1369-7021(11)70165-1.

[19] C. Liu, S. Luo, H. Huang, Y. Zhai, Z. Wang, Direct Growth of MoO_2/Reduced Graphene Oxide Hollow Sphere Composites as Advanced Anode Materials for Potassium-Ion Batteries. ChemSusChem. 12 (2019) 873-880. https://doi.org/10.1002/cssc.201802494

[20] H.J. Zhang, J. Shu, K.X. Wang, X.T. Chen, Y.M. Jiang, X. Wei, J.S. Chen, Lithiation mechanism of hierarchical porous MoO_2 nanotubes fabricated through one-step carbothermal reduction, J. Mater. Chem. A. 2 (2014) 80–86. https://doi.org/10.1039/c3ta14123c.

[21] Y. Sun, X. Hu, W. Luo, Y. Huang, Ultrafine MoO_2 nanoparticles embedded in a carbon matrix as a high-capacity and long-life anode for lithium-ion batteries, J. Mater. Chem. 22 (2012) 425–431. https://doi.org/10.1039/C1JM14701C.

[22] J.K. Shon, H.S. Lee, G.O. Park, J. Yoon, E. Park, G.S. Park, S.S. Kong, M. Jin, J.M. Choi,

H. Chang, S. Doo, J.M. Kim, W.S. Yoon, C. Pak, H. Kim, G.D. Stucky, Discovery of abnormal lithium-storage sites in molybdenum dioxide electrodes, Nat. Commun. 7 (2016) 1–9. https://doi.org/10.1038/ncomms11049.

[23] Y. Shi, B. Guo, S. a. Corr, Q. Shi, Y.-S. Hu, K.R. Heier, L. Chen, R. Seshadri, G.D. Stucky, Ordered Mesoporous Metallic MoO_2 Materials with Highly Reversible Lithium Storage Capacity, Nano Lett. 9 (2009) 4215–4220. https://doi.org/10.1021/nl902423a.

[24] X. Fang, B. Guo, Y. Shi, B. Li, C. Hua, C. Yao, Y. Zhang, Y.S. Hu, Z. Wang, G.D. Stucky, L. Chen, Enhanced Li storage performance of ordered mesoporous MoO_2 via tungsten doping., Nanoscale. 4 (2012) 1541–1544. https://doi.org/10.1039/c2nr12017h.

[25] Y. Sun, X. Hu, J.C. Yu, Q. Li, W. Luo, L. Yuan, W. Zhang, Y. Huang, Morphosynthesis of a hierarchical MoO_2 nanoarchitecture as a binder-free anode for lithium-ion batteries, Energy Environ. Sci. 4 (2011) 2870. https://doi.org/10.1039/c1ee01189h.

[26] H. Fu, Z. Xu, T. Wang, K. Li, X. Shen, J. Li, J. Huang, Rate behavior of MoO_2/graphene oxide lithium-ion battery anodes from electrochemical contributions, J. Electrochem. Soc. 165 (2018) 0–8. https://doi.org/10.1149/2.1271802jes.

[27] J. Wang, J. Polleux, J. Lim, B. Dunn, Pseudocapacitive Contributions to Electrochemical Energy Storage in TiO_2 (Anatase) Nanoparticles, J. Phys. Chem. C. 111 (2007) 14925–14931. https://doi.org/10.1021/jp074464w.

[28] M. Okubo, E. Hosono, J. Kim, M. Enomoto, N. Kojima, T. Kudo, H. Zhou, I. Honma, Nanosize effect on high-rate Li-ion intercalation in $LiCoO_2$ electrode, J. Am. Chem. Soc. 129 (2007) 7444–7452. https://doi.org/10.1021/ja0681927.

[29] B.K. Lesel, J.S. Ko, B. Dunn, S.H. Tolbert, Mesoporous $Li_xMn_2O_4$ Thin Film Cathodes for Lithium-Ion Pseudocapacitors, ACS Nano. 10 (2016) 7572–7581. https://doi.org/10.1021/acsnano.6b02608.

[30] K. Brezesinski, J. Wang, J. Haetge, C. Reitz, S.O. Steinmueller, S.H. Tolbert, B.M. Smarsly, B. Dunn, T. Brezesinski, Pseudocapacitive contributions to charge storage in highly ordered mesoporous group V transition metal oxides with iso-oriented layered nanocrystalline domains, J. Am. Chem. Soc. 132 (2010) 6982–6990. https://doi.org/10.1021/ja9106385.

[31] J.B. Cook, H.S. Kim, Y. Yan, J.S. Ko, S. Robbennolt, B. Dunn, S.H. Tolbert, Mesoporous MoS_2 as a Transition Metal Dichalcogenide Exhibiting Pseudocapacitive Li and Na-Ion Charge Storage, Adv. Energy Mater. (2016) 1–12. https://doi.org/10.1002/aenm.201501937.

[32] K. Brezesinski, J. Haetge, J. Wang, S. Mascotto, C. Reitz, A. Rein, S.H. Tolbert, J. Perlich, B. Dunn, T. Brezesinski, Ordered mesoporous α-Fe_2O_3 (Hematite) thin-film electrodes for application in high rate rechargeable lithium batteries, Small. 7 (2011) 407–414. https://doi.org/10.1002/smll.201001333.

[33] C. Largeot, C. Portet, J. Chmiola, P. Taberna, Y. Gogotsi, P. Simon, Relation between the Ion Size and Pore Size for an Electric Double-Layer Capacitor, J. Am. Chem. Soc. (2008) 2730–2731. https://doi.org/10.1016/j.carbon.2007.10.023.(15).

[34] I.E. Rauda, V. Augustyn, B. Dunn, S.H. Tolbert, Enhancing pseudocapacitive charge storage in polymer templated mesoporous materials, Acc. Chem. Res. 46 (2013) 1113–1124. https://doi.org/10.1021/ar300167h.

[35] J.B. Cook, H.S. Kim, T.C. Lin, S. Robbennolt, E. Detsi, B.S. Dunn, S.H. Tolbert, Tuning Porosity and Surface Area in Mesoporous Silicon for Application in Li-Ion Battery Electrodes, ACS Appl. Mater. Interfaces. 9 (2017) 19063–19073. https://doi.org/10.1021/acsami.6b16447.

[36] L. Zu, W. Zhang, L. Qu, L. Liu, W. Li, A. Yu, D. Zhao, Mesoporous materials for electrochemical energy storage and conversion. Adv. Energy. Mater. 10 (2020) 2002152. https://doi.org/10.1002/aenm.202002152

[37] A.B. Fuertes, F. Pico, J.M. Rojo, Influence of pore structure on electric double-layer capacitance of template mesoporous carbons, J. Power Sources. 133 (2004) 329–336. https://doi.org/10.1016/j.jpowsour.2004.02.013.

[38] G. O. Park, J. Yoon, S. B. Park, Z. Li, Y. S. Choi, W. S. Yoon, H. Kim, J. M. Kim, Nanostructural uniformity of ordered mesoporous materials: governing lithium storage behaviors. Small. 14 (2018) 1702985. https://doi.org/10.1002/smll.201702985

[39] T. Brezesinski, J. Wang, S.H. Tolbert, B. Dunn, Ordered mesoporous alpha-MoO_3 with iso-oriented nanocrystalline walls for thin-film pseudocapacitors., Nat. Mater. 9 (2010) 146–51. https://doi.org/10.1038/nmat2612.

[40] J.W. Kim, V. Augustyn, B. Dunn, The effect of crystallinity on the rapid pseudocapacitive response of Nb_2O_5, Adv. Energy Mater. 2 (2012) 141–148. https://doi.org/10.1002/aenm.201100494.

[41] J. Liu, Y. Lu, R. Wang, Z. Xu, X. Li, The effect of calcination temperature on combustion preparation of $ZnFe_2O_4$ as anode for lithium batteries. Int. J. Electrochem. Sci, 15 (2020) 1571-1580. https://doi: 10.20964/2020.02.43

[42] C.K. Tsung, J. Fan, N. Zheng, Q. Shi, A.J. Forman, J. Wang, G.D. Stucky, A general route to diverse mesoporous metal oxide submicrospheres with highly crystalline frameworks, Angew. Chemie - Int. Ed. 47 (2008) 8682–8686. https://doi.org/10.1002/anie.200802487.

[43] Y. Liu, X. Zhang, Effect of calcination temperature on the morphology and electrochemical properties of Co_3O_4 for lithium-ion battery, Electrochim. Acta. 54 (2009) 4180–4185. https://doi.org/10.1016/j.electacta.2009.02.060.

[44] B.K. Lesel, J.B. Cook, Y. Yan, T.C. Lin, S.H. Tolbert, Using Nanoscale Domain Size to Control Charge Storage Kinetics in Pseudocapacitive Nanoporous $LiMn_2O_4$ Powders, ACS Energy Lett. 2 (2017) 2293–2298. https://doi.org/10.1021/acsenergylett.7b00634.

[45] E.K. Richman, C.B. Kang, T. Brezesinski, S.H. Tolbert, Ordered mesoporous silicon through magnesium reduction of polymer templated silica thin films., Nano Lett. 8 (2008) 3075–9. https://doi.org/10.1021/nl801759x.

[46] T. Brezesinski, M. Groenewolt, N. Pinna, H. Amenitsch, M. Antonietti, B. Smarsly, Surfactant-Mediated Generation of Iso-Oriented Dense and Mesoporous Crystalline Metal-Oxide Layers, Adv. Mater. 18 (2006) 1827–1831. https://doi.org/10.1002/adma.200600154.

[47] T. Brezesinski, J. Wang, J. Polleux, B. Dunn, S.H. Tolbert, Templated nanocrystal-based porous TiO_2 films for next-generation electrochemical capacitors., J. Am. Chem. Soc. 131 (2009) 1802–9. https://doi.org/10.1021/ja8057309.

[48] R. Buonsanti, T.E. Pick, N. Krins, T.J. Richardson, B. a Helms, D.J. Milliron, Assembly of ligand-stripped nanocrystals into precisely controlled mesoporous architectures., Nano Lett. 12 (2012) 3872–7. https://doi.org/10.1021/nl302206s.

[49] I.E. Rauda, R. Buonsanti, L.C. Saldarriaga-Lopez, K. Benjauthrit, L.T. Schelhas, M. Stefik, V. Augustyn, J. Ko, B. Dunn, U. Wiesner, D.J. Milliron, S.H. Tolbert, General method for the synthesis of hierarchical nanocrystal-based mesoporous materials, ACS Nano. 6 (2012) 6386–6399. https://doi.org/10.1021/nn302789r.

[50] Q. Lu, J.G. Chen, J.Q. Xiao, Nanostructured electrodes for high-performance pseudocapacitors., Angew. Chem. Int. Ed. Engl. 52 (2013) 1882–9. https://doi.org/10.1002/anie.201203201.

[51] D.E. Cox, R.J. Cava, D.B. McWhan, D.W. Murphy, A neutron powder diffraction study of the lithium insertion compound $LiMoO_2$ from 4 - 440 K, J. Phys. Chem. Solids. 43 (1982) 657–666. https://doi.org/10.1016/0022-3697(82)90228-1.

[52] V. Augustyn, J. Come, M. a Lowe, J.W. Kim, P.-L. Taberna, S.H. Tolbert, H.D. Abruña, P. Simon, B. Dunn, High-rate electrochemical energy storage through Li^+ intercalation pseudocapacitance., Nat. Mater. 12 (2013) 518–22. https://doi.org/10.1038/nmat3601.

[53] J.-G.Kim, M.-S. Park, S.M. Hwang, Y.-U. Heo, T. Liao, Z. Sun, J.H. Park, K.J. Kim, G. Jeong, Y.-J. Kim, J.H. Kim, S.X. Dou, Zr^{4+} Doping in $Li_4Ti_5O_{12}$ anode for lithium-ion batteries: Open Li^+ diffusion paths through structural imperfection. ChemSusChem, 7 (2014) 1451-1457. https://doi.org/10.1002/cssc.201301393